NANO LETTERS

Letter

pubs.acs.org/NanoLett

Aligned Li^+ Tunnels in Core–Shell $Li(Ni_xMn_yCo_z)O_2$@$LiFePO_4$ Enhances Its High Voltage Cycling Stability as Li-ion Battery Cathode

Zhongzhen Wu,[†] Shunping Ji,[†] Tongchao Liu,[†] Yandong Duan,[†] Shu Xiao,[†] Yuan Lin,[†] Kang Xu,[‡] and Feng Pan*[,†]

[†]School of Advanced Materials, Peking University Shenzhen Graduate School, Shenzhen 518055, China

[‡]U.S. Army Research Laboratory, Adelphi, Maryland 20783, United States

Supporting Information

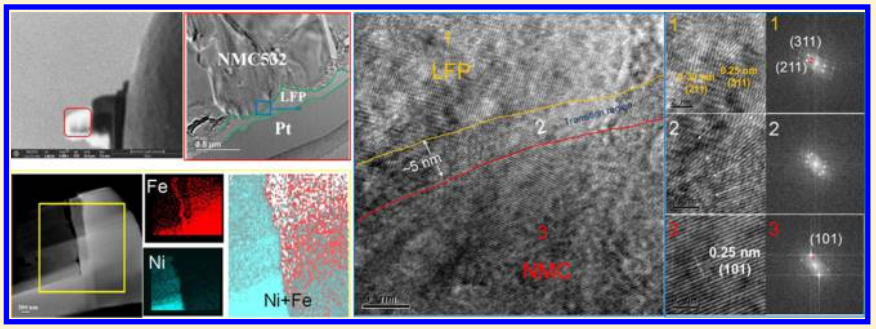

ABSTRACT: Layered transition-metal oxides ($Li[Ni_xMn_yCo_z]O_2$, NMC, or NMCxyz) due to their poor stability when cycled at a high operating voltage (>4.5 V) have limited their practical applications in industry. Earlier researches have identified Mn(II)-dissolution and some parasitic reactions between NMC surface and electrolyte, especially when NMC is charged to a high potential, as primarily factors responsible for the fading. In our previous work, we have achieved a capacity of NMC active material close to theoretical value and optimized its cycling performance by a depolarized carbon nanotubes (CNTs) network and an unique "pre-lithiation process" that generates an in situ organic coating (~40 nm) to prevent Mn(II) dissolution and minimize the parasitic reactions. Unfortunately, this organic coating is not durable enough during a long-term cycling when the cathode operates at a high potential (>4.5 V). This work attempts to improve the surface protection of the NMC532 particles by applying an active inorganic coating consisting of nanosized- and crystal-orientated $LiFePO_4$ (LFP) (about 50 nm, exposed (010) face) to generate a core–shell nanostructure of $Li(Ni_xMn_yCo_z)O_2$@$LiFePO_4$. Transmission electron microscopy (TEM) and etching X-ray photoelectron spectroscopy have confirmed an intimate contact coating (about 50 nm) between the original structure of NMC and LFP single-particle with atomic interdiffusion at the core–shell interface, and an array of interconnected aligned Li^+ tunnels are observed at the interface by cross-sectional high-resolution TEM, which were formed by ball-milling and then strictly controlling the temperature below 100 °C. Batteries based on this modified NMC cathode material show a high reversible capacity when cycled between 3.0 and 4.6 V during a long-term cycling.

KEYWORDS: *$Li(Ni_{0.5}Mn_{0.3}Co_{0.2})O_2$, nano-$LiFePO_4$, aligned Li^+ tunnels, core–shell coating*

Cathode materials based on layered transition-metal oxides of ternary composition ($Li[Ni_xMn_yCo_z]O_2$, NMC or NMCxyz) have been regarded as one of the most promising chemistries for lithium ion batteries due to their high power/energy densities, low cost, and low toxicity as compared with the earliest commercialized cathode $LiCoO_2$.[1−3] However, owing to poor cycling stability of NMC when charged to high potentials, only part of the promised energy density could be accessed as a result of the limited operating potential (~4.2 V). Some responsible factors have been identified as Mn(II)-dissolution at the high potentials (>4.5 V) and the oxidation of electrolytes thereat.[4−6] Various approaches including structure optimization,[7−11] lattice doping,[12,13] and surface coating[14,15] have been proposed. Among these, surface coating seems to be simple, economical and effective. However, the thickness of a coating is a critical factor because most of these coating materials are electrochemically inactive and electronically insulating, such as Al_2O_3, ZnO, TiO_2, and so forth. When such an inert layer is too thin, it cannot provide a sufficient protection against Mn(II)-dissolution and parasitic reactions of electrolytes, which would still occur on NMC particles that are not entirely covered;[16,17] when such a layer is too thick, it would compromise a cycling capacity and rate performance due to both low electronic conductivity and low lithium ions diffusivity.[18] In our previous work, we designed a composite cathode consisting of $LiNi_{0.5}Mn_{0.3}Co_{0.2}O_2$ (NMC532) as the active species that is depolarized with an interwoven network of

Received: July 3, 2016
Revised: August 28, 2016
Published: September 2, 2016

DOI: 10.1021/acs.nanolett.6b02742
Nano Lett. 2016, 16, 6357−6363

single-walled carbon nanotubes (SWCNT) and a high capacity (~250 mAh/g) close to its theoretical value was realized.[19] To better retain this high capacity, we further introduced an organic protective layer on the surface of NMC and SWCNT via an in situ prelithiation protocol. A good ionic conductivity of this coating was found and brought impressive cycling stability;[20] however, its durability against high potential (>4.5 V) during long-term cycling is still unsatisfactory, and an alternative protective layer with a higher stability against high potentials and reliability against long-term cycling must be considered.

In this work, we choose $LiFePO_4$ (LFP), which is an excellent active cathode material itself with electronically conductive and Li-ion conductive properties, as the candidate for such a coating, hoping its inorganic nature and excellent chemical stability up to 4.6 V[21] of both bulk and interface with organic electrolyte could provide a durable surface protection for NMC at high voltages. In the literature, no promising result has ever been achieved when LFP was attempted as a coating material on NMC.[22,23] In our opinion, there might be two rationales underneath those unsuccessful efforts: first, the large-sized of LFP particles have poor electronic conductivity and low surface free energy, thus limiting the thickness to be under certain value and causing incomplete coverage; and second in order to result in an intimate interfacial contact between LFP and NMC, a higher calcination temperature had to be applied, which may have practically destroyed the activity of the materials due to an interfacial reaction between NMC and LFP, leading to a nonintimate interface of a mismatch for Li^+ tunnels between the layered NMC core and the unidimensional Li^+ tunnels of LFP shell.

Herein, we try to circumvent these issues by using a nanosized and crystal orientated $LiFePO_4$ (nano-LFP, about 50 nm, exposed (010) face) as the coating material. Its larger surface energy and shorter ion/electron diffusion length, which weakens the effect of poor electronic conductivity, are expected to form a complete coverage and to enable a chemically and electrochemically durable thin layer. In addition, the smaller nano-LFP reduces the needed treatment temperature (≤100 °C) and maintains the original structures of NMC and LFP and such a (010)-face-orientated $LiFePO_4$ generates aligned Li^+ tunnels at the interface self-assembly. Lithium half cells based on this nano-LFP modified NMC materials exhibit both high reversible capacity and excellent cycling performance during a long-term cycling when charged/discharged between 3.0 and 4.6 V, which is a higher potential than that of ordinary NMC materials experience.

NMC532 and nanosized LFP materials were prepared in lab by coprecipitation and reflux route, respectively. Details of the processes are described in the Support Information. Schematic of the preparation process for LFP-coated NMC532 (denoted NMC@LFP hereafter) cathode electrode is shown in Figure 1. The mass contents of NMC@LFP were adjusted to be 5, 10, and 15 wt %, and they are denoted hereafter as NMC@LFP (5%), NMC@LFP (10%) and NMC@LFP (15%). Nano-LFP particles were coated on the surface of microsized NMC532 by electrostatic interactions under ball-milling rotation conditions with a rolling speed of 500 rpm for 5 h in a planetary ball miller (no grinding ball was used in order to prevent the structure destruction and interfacial reactions). Calcination was conducted at 100 °C for an hour to improve the adhesion between LFP and NMC532.

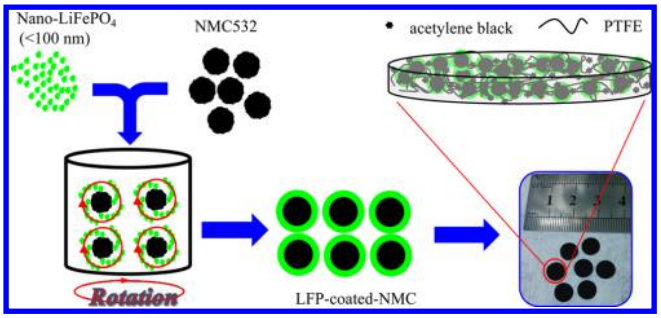

Figure 1. Schematic of the preparation process for LFP-coated-NMC cathode electrode.

Morphologies of NMC532, nano-LFP and NMC@LFP materials are analyzed by field emission scanning electron microscopy (FESEM), as shown in Figure 2. For pristine

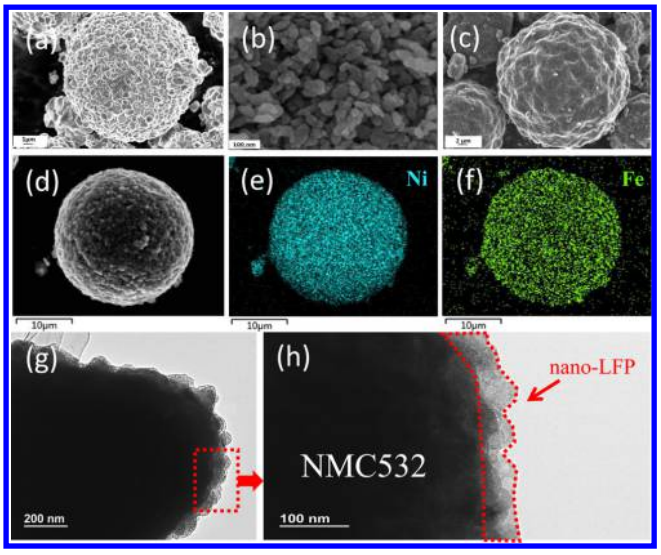

Figure 2. SEM images of (a) pristine NMC532 particles, (b) nano-LFP particles, (c) NMC@LFP(10%) and EDS mapping of NMC@LFP(10%) sample (d) SEM image, (e) Ni element, and (f) Fe element; (g) TEM images of NMC@LFP(10%) sample and (h) the magnified image of the corresponded area marked in the red square.

NMC532 (Figures 2a and S1b), the size of the secondary spherical particles comprising numerous sphere-like submicron particles reaches up to about 10 μm. Nano-LFP shows uniform ellipsoid-shaped grains with an average size of 50 nm (Figures 2 and S1a). The core−shell NMC@LFP particles are shown in Figures 2c and S1c and reveal a smoother surface than pristine NMC532. The elemental distribution and composition on the surface of the NMC@LFP samples were analyzed by energy dispersive spectroscopy (EDS), as shown in Figures 2e,f and S2. Ni, Co, Mn and Fe, P can be identified clearly. The distributions of Fe and P are complete and uniform on the surface of NMC532 particle, indicating a formation of nano-LFP coating layer and decreasing interface reactions between NMC particle surface and electrolyte are expected.[24] Thickness of nano-LFP layer is measured by TEM and is shown in Figure 2g,h, whose average thickness is about 50 nm, and agrees with the average size of the nano-LFP particles, indicating that this surface coating is essentially of single-particle thickness.

Cross-sectional high-resolution TEM test was performed to further reveal the details of the interface between NMC and

DOI: 10.1021/acs.nanolett.6b02742
Nano Lett. 2016, 16, 6357−6363

nano-LFP for NMC@LFP (10%) sample, as shown in Figure 3. A cross-sectional sample for observing high-resolution TEM

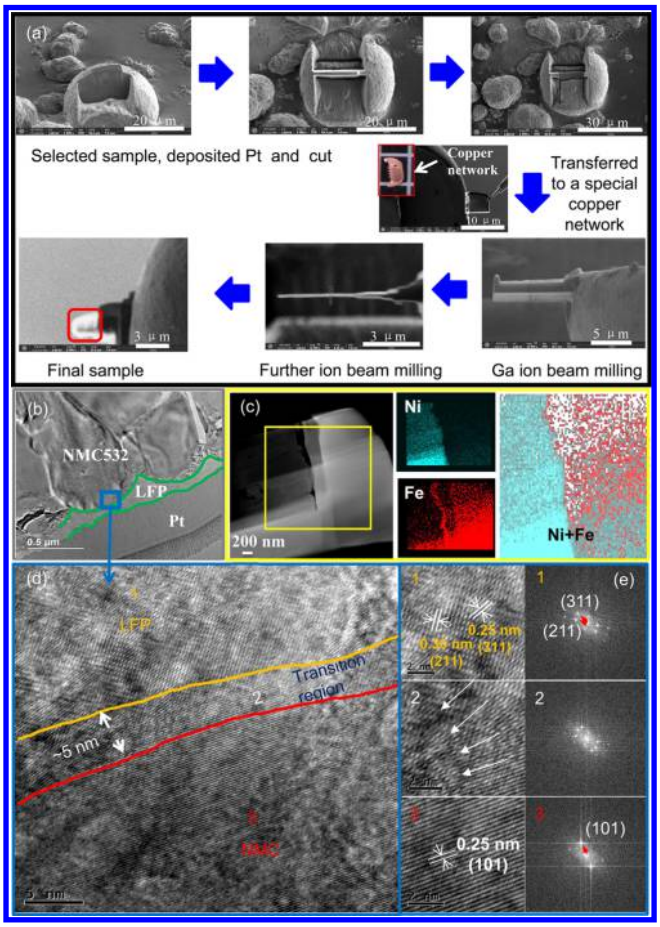

Figure 3. A brief introduction to preparing a cross-sectional high-resolution TEM sample by FIB (a) and the TEM images of the aligned Li^+ tunnels at the interface of the core−shell NMC@LFP(10%) materials. (b) TEM image of the interface, (c) the distributions of Ni and Fe at the interface, (d) high-resolution TEM image of the interface and (e) crystal lattice and electron diffraction images of the locations marked 1, 2, and 3 in (d).

was prepared by focused ion beam (FIB) and the detail process is indicated in Figure 3a and Supporting Information. The nano-LFP layer is clearly observed to be around the NMC surface in Figure 3b, and the distributions of Ni and Fe elements, representing NMC and LFP, respectively, are depicted by EDS elemental mappings in Figure 3c with both showing the same nanostructure as Figure 2. The lattice characteristics of the interface between the nano-LFP and NMC particles are described in Figure 3d, where three distinguished zones marked by the labels of 1, 2, and 3, respectively, can be differentiated from the orientations of their crystal planes. The crystal lattices and corresponding fast Fourier transform (FFT) algorithm results are shown in Figure 3e. The Zone 1 shows an orthorhombic space group *Pnma* with the *d*-spacing of 0.25 and 0.30 nm corresponding to LFP (311) and LFP (211) faces, respectively. The Zone 3 suggests a NMC (101) layered structure with the *d*-spacing of 0.25 nm.[25−27] Because of the approximately parallelism and the similar *d*-spacing between the LFP (211), LFP (311), and NMC (101), Zone 2 forms an interfacial transition region from LFP (211) and LFP (311) faces to NMC (101) face with width of about 5 nm. Within this transition region, the faces of LFP and NMC automatically aligned are observed, forming an array of interconnected tunnels for Li^+ between the core NMC particles and the nano-LFP shell.[28,29] Owing to (010)-face-orientated LFP was used as the coating materials in this research,[30] the exposed (010) face will be adsorbed onto the NMC surface under the external energy (ball-milling rotation conditions) for decreasing surface energy of NMC and nano-LFP particles. So, the cross-sectional HRTEM showed the LFP (211), (311) faces, which is approximately perpendicular to the exposed (010) face. Because of high surface free energy of nanoparticles and the lattice matching between LFP (311) and LFP (211) faces and NMC (101) face with similar *d*-spacing of 0.25 to 0.30 nm, a superlattice epitaxial growth that is familiar in the nanomultilayer films generates, as shown in the transition Zone 2.[31]

XRD patterns of the NMC532, nano-LFP, and NMC@LFP (5%, 10%, and 15%) samples are compared in Figure 4a. All diffraction peaks of NMC532 are well indexed with a layered α-$NaFeO_2$ structure with space group *R*3*m*. The marked splitting of these diffraction peaks ((006)/(102) and (108)/(110)) indicates its high ordering layered structure.[32,33] LFP shows a typical olivine structure with space group *Pnma*.[34] For NMC@LFP samples, the olivine structure emerges as the content of LFP reaches 10% and the peak intensities increase with the LFP contents. Except those indexed to the pristine NMC532 and LFP, no other obvious diffraction peaks can be detected, indicating that only strong interface interaction exists between pure phase of NMC532 and nano-LFP without new compounds generated.

In order to further understand the interface composition between pure phases of NMC532 and nano-LFP, the compositions dependence on the depth-profile of NMC@LFP (10%) are characterized by X-ray photoelectron spectroscopy (XPS, Figures 4b and S4). Ar^+-sputtering is employed to etch into the surface, and the data are collected at each 5 nm from the surface. Only the oxygen peak located at 531.2 eV, attributed to the binding energy of O 1s in nano-LFP, can be observed on the surface of the sample particles.[35] With increasing etching depth, a new oxygen peak appeared at 529.2 eV, originated from O 1s in NMC532, which becomes dominant when the etching thickness reaches up to 80 nm, indicating a gradual transition from the shell LFP to the core NMC532.[36] The evolutions of Fe, P, and Co and Mn and Ni with the etching showing in Figure S4 suggest the same nanoarchitecture. Note that around 40 nm depth etched, the decreases of Fe% synchronizes with the increase of Ni% and Mn%, which may result from atomic interdiffusion, including Li-ions diffusion from LFP to NMC caused by potential difference between LFP and MNC. In our previous work, we found once the vacancy of Li is generated during ball-milling, Fe can be induced to migrate,[37] which may lead to interdiffusion between the Fe atoms of LFP and Ni or/and Mn atoms of NMC532 near the interface that was formed by ball-milling and then calcinations at the strictly controlled low temperature (≤100 °C).

The thermal stability of LFP-NMC532 (10%) and possible interfacial reactions between the two layers are studied by differential scanning calorimetry (DSC), as shown in Figure 4c. No obvious thermal effect was found on the NMC532 material in the DSC curve from room temperature to 650 °C in Ar atmosphere. However, a large and wide endothermic peak was observed between 200 and 500 °C for the NMC@LFP,

DOI: 10.1021/acs.nanolett.6b02742
Nano Lett. 2016, 16, 6357−6363

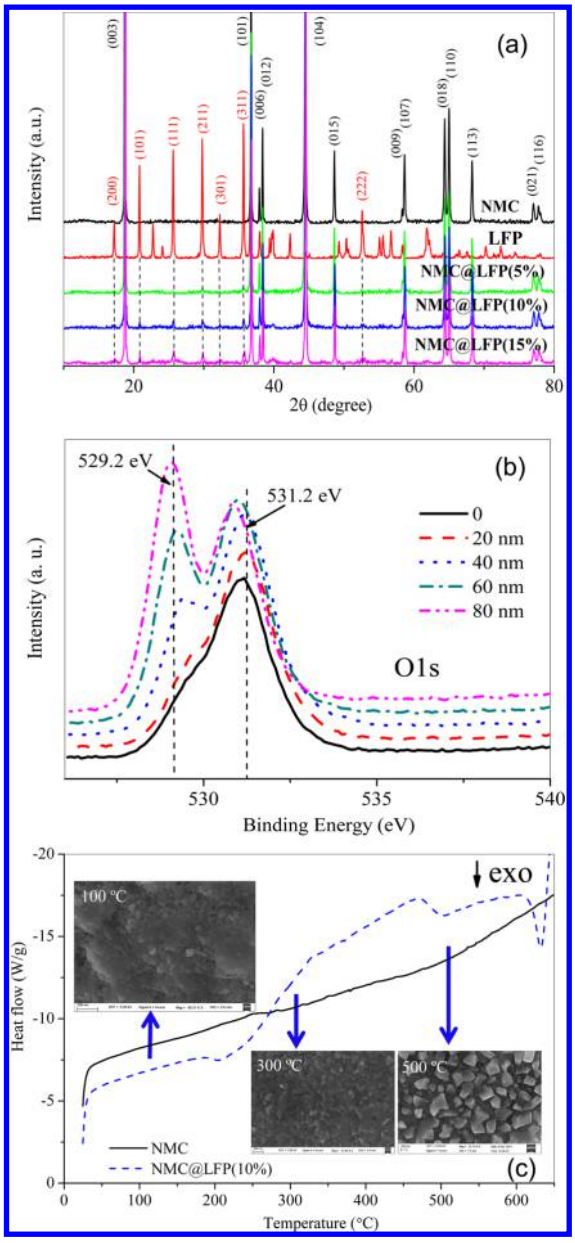

Figure 4. (a) XRD patterns of pristine NMC532, nano-LFP, NMC@LFP(5%), NMC@LFP(10%), and NMC@LFP(15%) samples, (b) etching XPS spectra of O 1s for NMC@LFP(10%) sample, and (c) DSC curves of NMC532 and NMC@LFP(10%) samples (inset are SEM images of NMC@LFP(10%) sample depending on temperatures).

indicating that some reactions happened between the two phases during heating, which provides us with rationale about the forming temperature range for the core−shell structure. Furthermore, the surface morphology of the NMC@LFP particles was also investigated by SEM as a function of the heating temperatures for 5 h, as shown in Figure 4c) (inset) and Figure S5, which shows no significant change under 100 °C. However, nano-LFP particles on the surface grew up apparently with increasing heating temperature, and the particles eventually became larger than 200 nm when the temperature reaches 500 °C. The corresponding compositions detected by energy dispersive spectroscopy (EDS), shown in Figure S6, indicates that the new grains, owning identical chemical composition with nano-LFP, are formed by crystallization and merging of the latter. In addition to nano-LFP growth, some side products were also identified by XRD when the temperature reaches 500 °C, indicating the destruction of the nano-LFP and NMC532 structures and the fall apart of interface as shown in Figure S7.

The first five cycles of the cyclic voltammograms for NMC532 and NMC@LFP (10%) materials are conducted at a sweep rate of 0.1 mV/s in the voltage range of 3.0−4.6 V, as shown in Figure 5a,b. Only one pair of cathodic/anodic peaks are observed for the NMC532 sample during a charge−discharge process, attributed to the redox process of Ni^{2+}/Ni^{4+}.[38] The initial cathodic/anodic peaks are centered at 4.37 V/3.70 V, corresponding to the Li^+-deintercalation/intercalation processes. However, in Figure 5b a new pair of cathodic/anodic peaks during the first cycle appeared at 3.60 V/3.36 V in NMC@LFP (10%), which corresponds to the Fe^{2+}/Fe^{3+} redox process, respectively. Note that the initial cathodic peak shifts to higher voltage about 0.2 V (3.60 V versus 3.4 V) compared with the second and more cycles and with pure LFP (see Figure S8), which should result from interface interaction under electrochemical process with Li^+ deintercalation around MNC@LFP interface layer with reconfiguration. Compared with the pristine NMC532, which delithiates at 4.37 V, the initial delithiation voltage (Ni^{2+}/Ni^{4+}) of the NMC@LFP (10%) sample is much lower at 4.16 V during the first cycle, indicating that the new types of interfacial reactions between LFP and NMC were occurred to generate the stable LFP coating interface layers with obvious depolarization for Li-ion diffusions on the oxidation of Ni during the first cycle.[39−41] The decreased overpotential suggests the similar depolarization effect as shown in Figure S9. Figure 5c compares the charge−discharge profiles for the pristine NMC532 and NMC@LFP (10%) at the 100th cycle in the voltage range of 3.0−4.5 V and at the rate of 1/3 C. Compared with the NMC532 that contains only Ni^{2+}/Ni^{4+} redox plateaus at about 3.7 V, an extra plateau can be seen at about 3.4 V, arising from the Fe^{2+}/Fe^{3+} redox of LFP. The electrochemical impedance spectra are used to investigate the effect of nano-LFP and the interface to NMC532 materials in high voltage cycling performance. The Nyquist plots of NMC532 and NMC@LFP (10%) after 5th, 50th, and 100th cycles at the charge state of 4.6 V are summarized in Figure 5d. These plots are composed by two semicircles at the high- and medium-frequency regions, respectively, and an oblique line at the low-frequency region. The corresponding equivalent circuit is represented in Figure S10, where the intercept at high frequency corresponds to uncompensated ohmic resistance (R_s), the two semicircles in the high- and medium-frequency regions correspond to the resistances R_f (solid electrolyte interface (SEI) layer and the surface-modified layer) and R_{ct} (charge-transfer in the electrolyte/electrode interface), respectively, and the oblique line in the low-frequency stands for Warburg impedance Zw induced by Li^+ diffusion in the bulk material.[42−44] All data derived from equivalent circuits are listed in Table S1. R_s of all samples slightly increases with the increase of SOC cycles, while R_f and R_{ct} of pristine NMC532 are significantly higher than those of NMC@LFP, indicating that the presence of a nano-LFP coating hinders the side reactions between NMC and electrolyte, and subsequently reduces the interfacial resistance to charge (Li^+ and electron) transport. This should eventually be reflected in the improved electrochemical performances when cycled at high voltages.

DOI: 10.1021/acs.nanolett.6b02742
Nano Lett. 2016, 16, 6357−6363

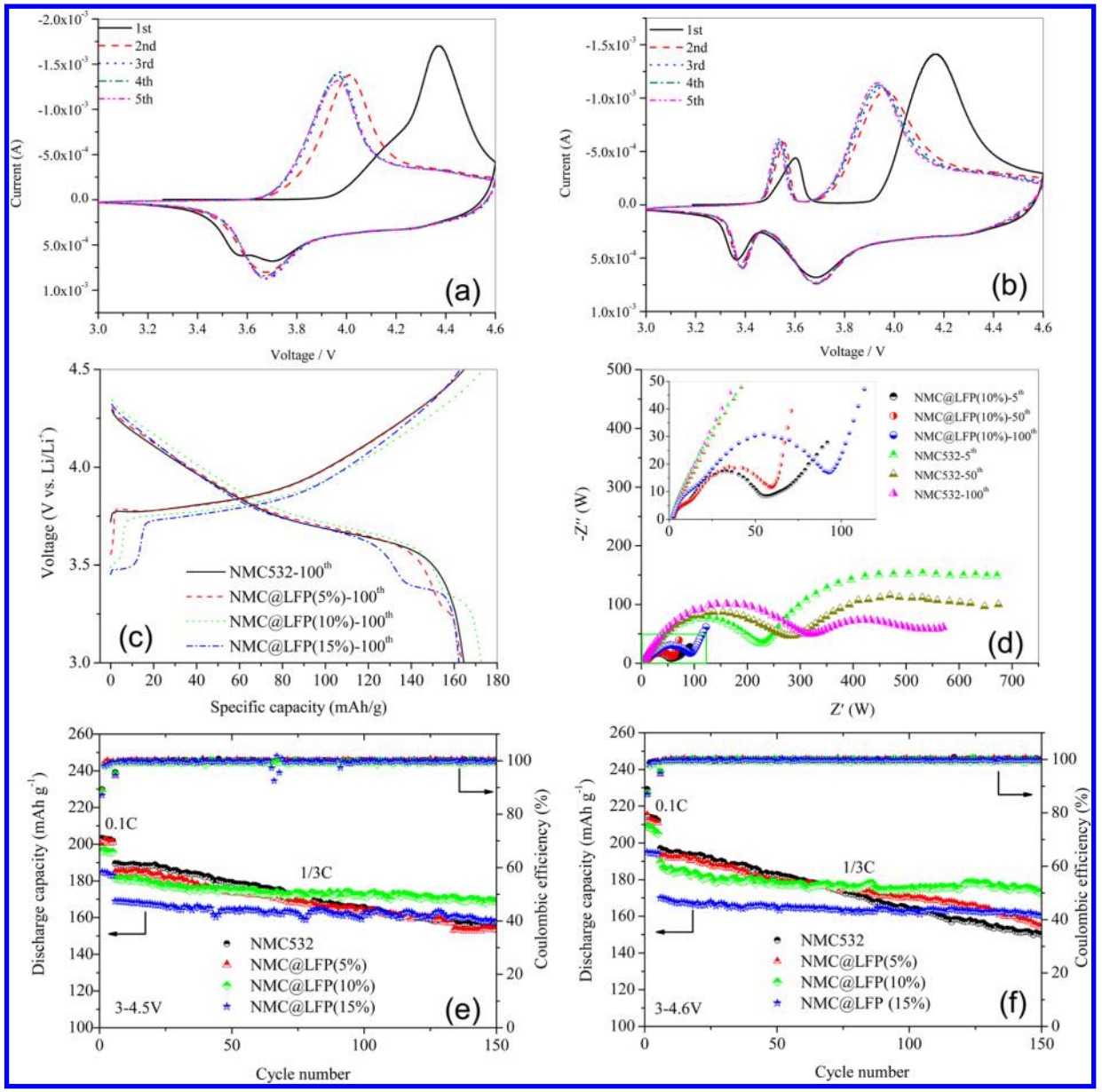

Figure 5. CV curves of (a) pristine NMC532 and (b) NMC@LFP(10%) with a scan rate of 0.1 mV/s in the voltage range of 3.0−4.6 V, (c) the 100th charge−discharge curves of samples between 3.0 and 4.5 V at 1/3 C, and (d) Nyquist plots of NMC532 and NMC@LFP(10%) at a charge state of 4.6 V for the 5th, 50th, and 100th cycles, the cycling performance of pristine NMC532 and NMC@LFP(5,10,15%) at 0.1 and 1/3 C rate in the voltage range of (e) 3.0−4.5 and (f) 3.0−4.6 V.

Figure 5e,f shows the cycling performance of the pristine NMC532 and NMC@LFP samples with different nano-LFP mass contents in the voltage range of 3.0−4.5 V and 3.0−4.6 V with the rate of 0.1 C and 1/3 C at room temperature. The first discharge capacities of the NMC532, NMC@LFP(5%), NMC@LFP(10%), and NMC@LFP(15%) were 189.7, 184.8, 181.5, and 169.6 mAh/g , respectively, in the voltage range of 3.0−4.5 V at 1/3 C rate. The first discharge capacities of the NMC@LFP samples decrease gradually with the increasing content of nano-LFP, which may attribute to the lower theoretical capacity of LFP compared with that of NMC. However, the discharge capacity of NMC532 declines at much faster pace and only 155.4 mAh/g remains (18.1% capacity loss) after 150 cycles. The cycling stability is apparently improved when the NMC532 is protected by a nano-LFP coating. The optimized content of nano-LFP is found to be 10%, and the discharge capacity retains 168.5 mAh/g (only 7.2% capacity loss) after 150 cycles. Similarly, when the charging voltage increases to 4.6 V, as shown in Figure 5f), the discharge capacity of the pristine NMC532 declines to 150 mAh/g after 150 cycles with about 23.9% loss compared with the initial value. The optimized NMC@LFP (10%), however, retains 173.3 mAh/g after 150 cycles, with 8.5% capacity loss (a fluctuation error of 2.9% relative to the mean value) compared with the initial value. All the results suggest that the high-voltage cycling performance of the NMC532 material can be effectively improved through nano-LFP coating, which suppresses the dissolution of Mn in the electrolyte confirmed by inductively coupled plasma−atomic emission spectroscopy during a long-term cycling (shown in Table S2) and there is an optimized nano-LFP content. On the other hand, excessive amounts of LFP are expected to be detrimental to the diffusion

DOI: 10.1021/acs.nanolett.6b02742
Nano Lett. 2016, 16, 6357−6363

of electrons and ions and subsequently lead to compromises in capacity and cycling stability.

In order to construct a durable coating on the NMC particles to prevent the parasitic reactions between NMC materials and electrolyte, nano-LFP is used to modify the surface of NMC532 material completely and uniformly by ball-milling rotation at a low temperature. Studies on the coating conditions indicates that nanosized LFP and the coating temperature (under 100 °C) seem to be critical factors to ensure an interface that facilitates diffusion of both ions and electrons as well as maintains the original structures and interfacial connecting. Compared with that of pristine NMC532, NMC@LFP (10%) with the designed and optimized nano-LFP coating shows the superior cycling stability with the discharge capacity of 168.5 mAh/g (7.2% capacity loss) and 173.3 mAh/g (8.5% capacity loss) retained after 150 cycles when charging/discharging between 3.0 and 4.5 V and between 3.0 and 4.6 V at 1/3 C, respectively. The improvements in the reversible capacity utilization and long-term cycling stability as the result of a durable inorganic coating (nano-LFP) suggests an effective approach to circumvent the intrinsic disadvantages of NMC-based materials, further promoting their possibility for practical applications in electric vehicles.

■ ASSOCIATED CONTENT

Supporting Information

The Supporting Information is available free of charge on the ACS Publications website at DOI: 10.1021/acs.nanolett.6b02742.

Experimental section, morphology of the original modified materials and those heating in different temperatures, compositions, XPS spectra, XRD patterns, and Nyquist plots of the prepared samples (PDF)

■ AUTHOR INFORMATION

Corresponding Author

*Tel/Fax: +86-755-26033200. E-mail: panfeng@pkusz.edu.cn.

Author Contributions

Z.W. and S.J. contributed equally to this work.

Notes

The authors declare no competing financial interest.

■ ACKNOWLEDGMENTS

This work was financially supported jointly by National Science Foundation of China (51301004), Guangdong Innovation Team Project (2013N080) and Shenzhen Science and Technology Research Grant (JCYJ20140903102215536, JCYJ20150828093127698, CXZZ20120829172325895, peacock plan KYPT20141016105435850).

■ REFERENCES

(1) Tarascon, J. M.; Armand, M. *Nature* **2001**, *414*, 359−367.
(2) Whittingham, M. S. *Chem. Rev.* **2004**, *104*, 4271−4302.
(3) Dunn, B.; Kamath, H.; Tarascon, J. M. *Science* **2011**, *334*, 928−935.
(4) Zhan, C.; Lu, J.; Kropf, A. J.; Wu, T.; Jansen, A. N.; Sun, Y. K.; Qiu, X.; Amine, K. *Nat. Commun.* **2013**, *4*, 2437.
(5) Wang, L.; Li, J.; He, X.; Pu, W.; Wan, C.; Jiang, C. *J. Solid State Electrochem.* **2009**, *13*, 1157−1164.
(6) Jiang, M.; Key, B.; Meng, Y. S.; Grey, C. P. *Chem. Mater.* **2009**, *21*, 2733−2745.
(7) Sun, Y. K.; Chen, Z.; Noh, H. J.; Lee, D. J.; Jung, H. G.; Ren, Y.; Wang, S.; Yoon, C. S.; Myung, S. T.; Amine, K. *Nat. Mater.* **2012**, *11*, 942−947.
(8) Zhang, L. J.; Li, N.; Wu, B. R.; Xu, H. L.; Wang, L.; Yang, X. Q.; Wu, F. *Nano Lett.* **2015**, *15*, 656−661.
(9) Cho, Y.; Oh, P.; Cho, J. *Nano Lett.* **2013**, *13*, 1145−1152.
(10) Hou, P. Y.; Wang, X. Q.; Wang, D. G.; Song, D. W.; Shi, X. X.; Zhang, L. Q.; Guo, J.; Zhang. *RSC Adv.* **2014**, *4*, 15923−15929.
(11) Hou, P. Y.; Wang, X. Q.; Song, D. W.; Shi, X. X.; Zhang, L. Q.; Guo, J.; Zhang, J. *J. Power Sources* **2014**, *265*, 174−181.
(12) Gong, C. X.; Lv, W. X.; Qu, L. M.; Bankole, O. E.; Li, G. H.; Zhang, R.; Hu, M.; Lei, L. X. *J. Power Sources* **2014**, *247*, 151−155.
(13) Croguennec, L.; Bains, J.; Bréger, J.; Tessier, C.; Biensan, P.; Levasseur, S.; Delmas, C. *J. Electrochem. Soc.* **2011**, *158*, A664−A670.
(14) Konishi, H.; Yoshikawa, M.; Hirano, T. *J. Power Sources* **2013**, *244*, 23−28.
(15) Lee, Y.-S.; Shin, W.-K.; Kannan, A. G.; Koo, S. M.; Kim, D.-W. *ACS Appl. Mater. Interfaces* **2015**, *7*, 13944−13951.
(16) Bai, Y.; Wang, X.; Yang, S.; Zhang, X.; Yang, X.; Shu, H.; Wu, Q. *J. Alloys Compd.* **2012**, *541*, 125−131.
(17) Su, Y.; Cui, S.; Zhuo, Z.; Yang, W.; Wang, X.; Pan, F. *ACS Appl. Mater. Interfaces* **2015**, *7*, 25105−25109.
(18) Liu, X.-H.; Kou, L.-Q.; Shi, T.; Liu, K.; Chen, L. *J. Power Sources* **2014**, *267*, 874−880.
(19) Wu, Z.; Han, X.; Zheng, J.; Wei, Y.; Qiao, R.; Shen, F.; Dai, J.; Hu, L.; Xu, K.; Lin, Y.; Yang, W.; Pan, F. *Nano Lett.* **2014**, *14*, 4700−4706.
(20) Wu, Z.; Ji, S.; Zheng, J.; Hu, Z.; Xiao, S.; Wei, Y.; Zhuo, Z.; Lin, Y.; Yang, W.; Xu, K.; Amine, K.; Pan, F. *Nano Lett.* **2015**, *15*, 5590−5596.
(21) Kim, J. K.; Cheruvally, G.; Ahn, J. H. *J. Solid State Electrochem.* **2008**, *12*, 799−805.
(22) Kim, W.-S.; Kim, S.-B.; Jang, I. C.; Lim, H. H.; Lee, Y. S. *J. Alloys Compd.* **2010**, *492*, L87−L90.
(23) Kim, S.-B.; Lee, K. J.; Choi, W. J.; Kim, W.-S.; Jang, I. C.; Lim, H. H.; Lee, Y. S. *J. Solid State Electrochem.* **2010**, *14*, 919−922.
(24) Lin, F.; Markus, I. M.; Nordlund, D.; Weng, T.-C.; Asta, M. D.; Xin, H. L.; Doeff, M. M. *Nat. Commun.* **2014**, *5*, 3529.
(25) Nan, C.; Lu, J.; Chen, C.; Peng, Q.; Li, Y. *J. Mater. Chem.* **2011**, *21*, 9994−9996.
(26) Jung, S.-K.; Gwon, H.; Hong, J.; Park, K.-Y.; Seo, D.-H.; Kim, H.; Hyun, J.; Yang, W.; Kang, K. *Adv. Energy Mater.* **2014**, *4*, 1300787.
(27) Wang, L.; He, X.; Sun, W.; Wang, J.; Li, Y.; Fan, S. *Nano Lett.* **2012**, *12*, 5632−5636.
(28) Hou, P.; Wang, X.; Wang, D.; Song, D.; Shi, X.; Zhang, L.; Guo, J.; Zhang, J. *RSC Adv.* **2014**, *4*, 15923−15929.
(29) Wang, Z.; Huang, S.; Chen, B.; Wu, H.; Zhang, Y. *J. Mater. Chem. A* **2014**, *2*, 19983−19987.
(30) Zheng, J.; Hou, Y.; Duan, Y.; Song, X.; Wei, Y.; Liu, T.; Hu, J.; Guo, H.; Zhuo, Z.; Liu, L.; Chang, Z.; Wang, X.; Zherebetskyy, D.; Fang, Y.; Lin, Y.; Xu, K.; Wang, L. W.; Wu, Y.; Pan, F. *Nano Lett.* **2015**, *15*, 6102−6109.
(31) Sproul, W. D. *Science* **1996**, *273*, 889−892.
(32) Kang, S.-H.; Kim, J.; Stoll, M. E.; Abraham, D.; Sun, Y. K.; Amine, K. *J. Power Sources* **2002**, *112*, 41−48.
(33) Li, D.; Sasaki, Y.; Kageyama, M.; Kobayakawa, K.; Sato, Y. *J. Power Sources* **2005**, *148*, 85−89.
(34) Gwon, H.; Seo, D.-H.; Kim, S.-W.; Kim, J.; Kang, K. *Adv. Funct. Mater.* **2009**, *19*, 3285−3292.
(35) Kanamura, K.; Shiraishi, S.; Tamura, H.; Takehara, Z.-I. *J. Electrochem. Soc.* **1994**, *141*, 2379−2385.
(36) Kong, J.-Z.; Zhai, H.-F.; Ren, C.; Tai, G.-A.; Yang, X.-Y.; Zhou, F.; Li, H.; Li, J.-X.; Tang, Z. *J. Solid State Electrochem.* **2014**, *18*, 181−188.
(37) Guo, H.; Song, X.; Zhuo, Z.; Hu, J.; Liu, T.; Duan, Y.; Zheng, J.; Chen, Z.; Yang, W.; Amine, K.; Pan, F. *Nano Lett.* **2016**, *16*, 601−608.
(38) Park, S. H.; Yoon, C. S.; Kang, S. G.; Kim, H. S.; Moon, S. I.; Sun, Y. K. *Electrochim. Acta* **2004**, *49*, 557−563.

DOI: 10.1021/acs.nanolett.6b02742
Nano Lett. 2016, 16, 6357−6363

(39) Liu, T.; Zhao, S.-X.; Wang, K. Z.; Nan, C.-W. *Electrochim. Acta* **2012**, *85*, 605−611.
(40) Liu, X.-H.; Kou, L.-Q.; Shi, T.; Liu, K.; Chen, L. *J. Power Sources* **2014**, *267*, 874−880.
(41) Liu, L.; Yan, X.; Wang, Y.; Zhang, D.; Du, F.; Wang, C.; Chen, G.; Wei, Y. *Ionics* **2014**, *20*, 1087−1093.
(42) Huang, Y. Y.; Chen, J. T.; Ni, J. P.; Zhou, H. H.; Zhang, X. X. *J. Power Sources* **2009**, *188*, 538−545.
(43) Liu, J.; Manthiram, A. *J. Mater. Chem.* **2010**, *20*, 3961−3967.
(44) Liu, J.; Wang, Q.; Reeja-Jayan, B.; Manthiram, A. *Electrochem. Commun.* **2010**, *12*, 750−753.

DOI: 10.1021/acs.nanolett.6b02742
Nano Lett. 2016, 16, 6357−6363